

Creative Commons Attribution 4.0 International (CC BY 4.0)

<https://creativecommons.org/licenses/by/4.0/>

Access to this work was provided by the University of Maryland, Baltimore County (UMBC) ScholarWorks@UMBC digital repository on the Maryland Shared Open Access (MD-SOAR) platform.

Please provide feedback

Please support the ScholarWorks@UMBC repository by emailing scholarworks-group@umbc.edu and telling us what having access to this work means to you and why it's important to you. Thank you.



High-velocity Blue-shifted Fe XXV He α Line during a Superflare of the RS Canum Venaticorum–type Star IM Peg

Shun Inoue¹, Wataru Buz Iwakiri², Teruaki Enoto^{1,3}, Hiroyuki Uchida¹, Miki Kurihara^{4,5}, Masahiro Tsujimoto⁵, Yuta Notsu^{6,7}, Kenji Hamaguchi^{8,9}, Keith Gendreau¹⁰, Zaven Arzoumanian¹⁰, and Takeshi Go Tsuru¹

¹Department of Physics, Kyoto University, Kitashirakawa-Oiwake-cho, Sakyo-ku, Kyoto, 606-8502, Japan; inoue@cr.scphys.kyoto-u.ac.jp

²International Center for Hadron Astrophysics, Chiba University, Inage-ku, Chiba, 263-8522, Japan

³RIKEN Cluster for Pioneering Research, 2-1 Hirosawa, Wako, Saitama, 351-0198, Japan

⁴Department of Astronomy, Graduate School of Science, The University of Tokyo, 7-3-1 Hongo, Bunkyo-ku, Tokyo 113-0033, Japan

⁵Japan Aerospace Exploration Agency, Institute of Space and Astronautical Science, Chuo-ku, Sagami-hara, Kanagawa 252-5210, Japan

⁶Laboratory for Atmospheric and Space Physics, University of Colorado Boulder, 3665 Discovery Drive, Boulder, CO 80303, USA

⁷National Solar Observatory, 3665 Discovery Drive, Boulder, CO 80303, USA

⁸CRESST II and X-ray Astrophysics Laboratory, NASA's Goddard Space Flight Center, Greenbelt, MD 20771, USA

⁹Department of Physics, University of Maryland, Baltimore County, Baltimore, MD, USA

¹⁰Astrophysics Science Division, NASA's Goddard Space Flight Center, Greenbelt, MD 20771, USA

Received 2024 May 20; revised 2024 June 7; accepted 2024 June 10; published 2024 June 26

Abstract

The Monitor of All-sky X-ray Image (MAXI) detected a superflare, releasing 5×10^{37} erg in 2–10 keV, of the RS CVn-type star IM Peg at 10:41 UT on 2023 July 23 with its Gas Slit Camera (2–30 keV). We conducted X-ray follow-up observations of the superflare with the Neutron Star Interior Composition Explorer (NICER; 0.2–12 keV) starting at 16:52 UT on July 23 until 06:00 UT on August 2. NICER X-ray spectra clearly showed emission lines of the Fe XXV He α and Fe XXVI Ly α for ~ 1.5 days since the MAXI detection. The Fe XXV He α line was blueshifted with its maximum Doppler velocity reaching -2200 ± 600 km s $^{-1}$, suggesting an upward-moving plasma during the flare, such as a coronal mass ejection (CME) and/or chromospheric evaporation. This is the first case that the Fe XXV He α line is blueshifted during a stellar flare, and its velocity overwhelmingly exceeds the escape velocity of the star (-230 km s $^{-1}$). One hour before the most pronounced blueshift detection, a signature of the reheating of the flare plasma was observed. We discuss the origin of the blueshift, a CME, or high-velocity chromospheric evaporation.

Unified Astronomy Thesaurus concepts: X-ray astronomy (1810); Stellar coronae (305); Stellar activity (1580); Stellar flares (1603); Stellar mass loss (1613)

1. Introduction

Stellar magnetic activity, such as flares and coronal mass ejections (CMEs), and their effects on exoplanets have recently attracted wide attention (e.g., Airapetian et al. 2020). One particular observational advance over the past decade is the increase of measurements of prominence eruptions, the initial interval of stellar CMEs. Optical spectroscopic observations revealed “blueshifts” or “blue asymmetries” of chromospheric lines, which are attributed to prominence eruptions (Vida et al. 2016; Flores Soriano & Strassmeier 2017; Fuhrmeister et al. 2018; Honda et al. 2018; Vida et al. 2019; Muheki et al. 2020a, 2020b; Koller et al. 2021; Maehara et al. 2021; Lu et al. 2022; Namekata et al. 2021; Inoue et al. 2023; Notsu et al. 2024; Namekata et al. 2024; Inoue et al. 2024). However, the information of the chromospheric lines is limited to the initial interval of mass ejection (Sinha et al. 2019). Optical observations alone cannot determine whether the erupted prominence eventually develops into a CME, escaping from the star. Thus, it is essential to observe X-ray lines, which have the information of the motion of CMEs.

So far, there are only two X-ray studies detecting the blueshifts caused by the plasma flow during a stellar flare (Argiroffi et al. 2019; Chen et al. 2022). Both observations were

conducted by the High-Energy Transmission Grating (HETG; Canizares et al. 2005) on the Chandra X-ray Observatory (Weisskopf et al. 2000). The stars whose blueshifts Argiroffi et al. (2019) and Chen et al. (2022) reported were the G-type star HR9024 and M-type star EV Lac, respectively. The reported velocity of blueshifts is ~ -100 km s $^{-1}$, below the escape velocity at the star surface. Both Argiroffi et al. (2019) and Chen et al. (2022) discussed the formation temperatures of the lines and discussed whether the blueshifts are attributed to a CME or chromospheric evaporation (Fisher et al. 1985). However, since these HETG studies investigated only the lines formed at temperatures below 20 MK (~ 1.7 keV), it was not known whether high-temperature (>50 MK) lines such as the Fe XXV He α and Fe XXVI Ly α are blueshifted during flares. On the solar flares, such high-temperature (>50 MK) plasma is thought to be formed above the top of a flare loop and related to the particle acceleration (Caspi 2010).

Large flares with energy exceeding 10^{35} erg from magnetically active RS CVn-type stars have been observed at both X-ray and visible wavelengths (e.g., Tsuru et al. 1989; Tsuboi et al. 2016; Sasaki et al. 2021; Inoue et al. 2023). Inoue et al. (2023) reported a prominence eruption during a flare releasing 7×10^{35} erg in the RS CVn-type star V1355 Orionis, whose outward velocity was measured to be 1600 km s $^{-1}$ by H α observations. On the other hand, no blueshifted X-ray lines have been reported despite many X-ray observations of RS CVn-type stars (e.g., Testa et al. 2004). The good photon



Original content from this work may be used under the terms of the [Creative Commons Attribution 4.0 licence](https://creativecommons.org/licenses/by/4.0/). Any further distribution of this work must maintain attribution to the author(s) and the title of the work, journal citation and DOI.

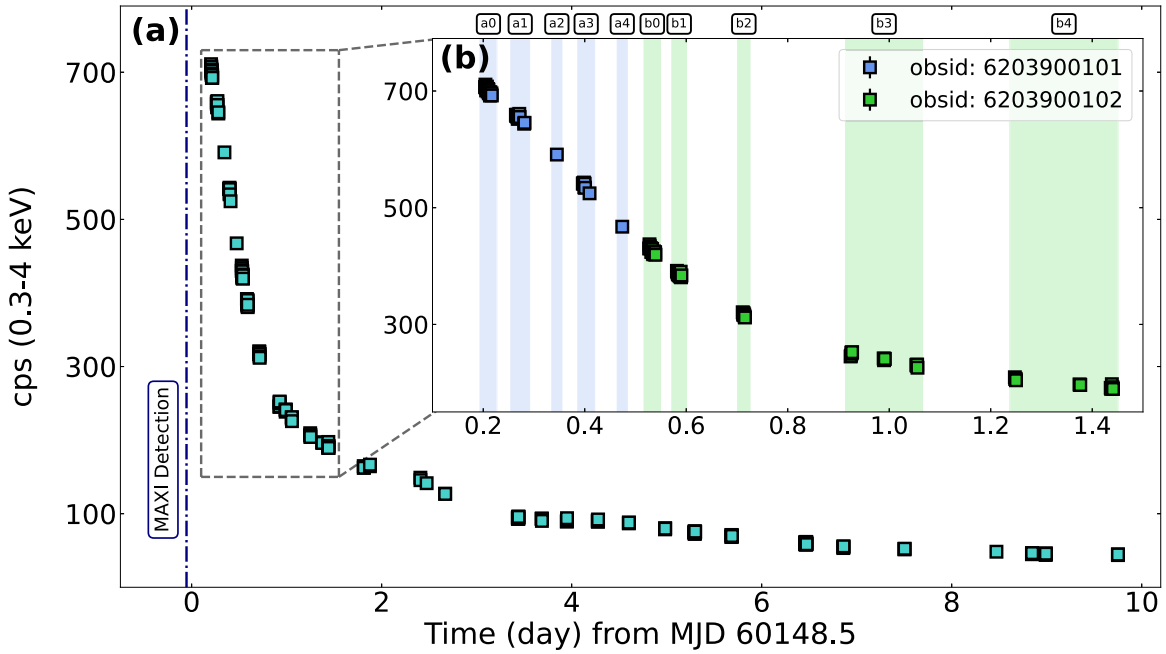


Figure 1. (a) 64 s binned 0.3–4 keV count rate (cps; counts s⁻¹) during all NICER observations of IM Peg. The time zero of MJD 60148.5 corresponds to 12:00 UT 2023 July 23. The one standard deviation statistical error bars are smaller than the symbol size. The navy vertical dashed–dotted line indicates the time when MAXI detected the flare (~ -0.05 day). (b) Enlarged light curve during the first two ObsIDs 6203900101 (blue) and 6203900102 (green). Interval numbers in our spectral analysis are shown above the inset panel.

statistics of large flares from RS CVn-type stars could allow us to statistically investigate a blueshift of the Fe XXV He α line.

In this Letter, we report the X-ray observation of a superflare from the RS CVn-type star IM Peg with the Neutron Star Interior Composition Explorer (NICER; Gendreau et al. 2016). The large effective area of NICER (600 cm² at 6 keV; Gendreau et al. 2012; Arzoumanian et al. 2014) allows us to conduct time-resolved spectral analysis during flares. We describe observation and data reduction (Section 2), results and discussion (Section 3), and conclusion (Section 4). In this Letter, the error ranges indicate 90% confidence level unless otherwise indicated.

2. Observation and Data Reduction

IM Peg is a well-known, active RS CVn-type star (e.g., Buzasi et al. 1987), whose basic parameters are summarized in Table 1 of Zellem et al. (2010), e.g., the stellar mass and radius of this K-type star are $M=1.8M_{\odot}$ and $R=13.3R_{\odot}$, respectively, where M_{\odot} and R_{\odot} are the mass and radius of the Sun, respectively. The corresponding escape velocity at the stellar surface is $v_e = \sqrt{2GM/R} = 230$ km s⁻¹. This long-period RS CVn binary consists of K2 III + G4V stars with an orbital period of 24.6 days. The K2 III star has synchronized rotation and is heavily spotted and the likely source of the superflare.

The Monitor of All-sky X-ray Image (MAXI; Matsuoka et al. 2009) detected a flare from IM Peg at 10:41 UT on 2023 July 23. This flare was classified as a superflare by the radiated energy of 5×10^{37} erg in 2–10 keV (Iwakiri et al. 2023). We carried out follow-up observations with NICER from 16:52 UT on July 23 to 06:00 UT on August 2.

We downloaded the NICER data of ObsIDs: 6203900101–6203900111 from the HEASARC archive. We employed the standard analysis procedure. First, we used `nicerl2` in HEASoft ver. 6.32.1 to filter and calibrate raw data using the

calibration database version `xti20221001` with two options, which were (a) overshoot count rate range of 0–5; and (b) cut-off rigidity greater than 1.5 GeV c⁻¹. Then, we extracted light curves from the filtered events with `xselect` and generated ObsID-averaged source and background spectra with `nicerl3-spect` and the 3C50 model (Remillard et al. 2022). We also extracted time-resolved spectra of ObsIDs 6203900101 and 6203900102 with `nimaketime`, `niextract-event`, and `nicerl3-spect`. We used Xspec ver. 12.12.1 (Arnaud 1996) and PyXspec ver. 2.1.0 (Gordon & Arnaud 2021) for our spectral analyses.

3. Analysis and Result

Figure 1 shows the 0.3–4 keV light curve of all NICER observations of IM Peg covering the decay phase of the flare for ~ 10 days. We divided the first two ObsIDs 6203900101 and 6203900102 into good time intervals (GTIs) with their typical exposures of 500–1500 s. These GTIs are numbered as the intervals a0–b4 (Figure 1(b)). We combined the three GTIs of the intervals b3 and b4 to obtain better statistics for the following spectral analysis.

First, we extracted two spectra from the intervals a0–a4 and b0–b4 (Figure 2). We fit the wide-band (0.3–9 keV) spectra with a collisionally ionized equilibrium (CIE) model composed of three temperature components (`vapex+vapex+vapex`) convolved with interstellar absorption (`tbabs`). We tied the abundance among the three components. The best-fit temperatures of the three components for intervals a0–a4 and b0–b4 were 92 MK, 15 MK, and 0.92 MK and 64 MK, 13 MK, and 0.92 MK, respectively.

The Fe XXV He α and Fe XXVI Ly α lines were clearly detected during the intervals a0–a4 and b0–b4 (Figure 2), as expected from the temperatures (92 MK for a0–a4; 64 MK for b0–b4) of the hottest plasma components (Smith et al. 2001). The NICER energy resolution of 137 eV at 6 keV cannot

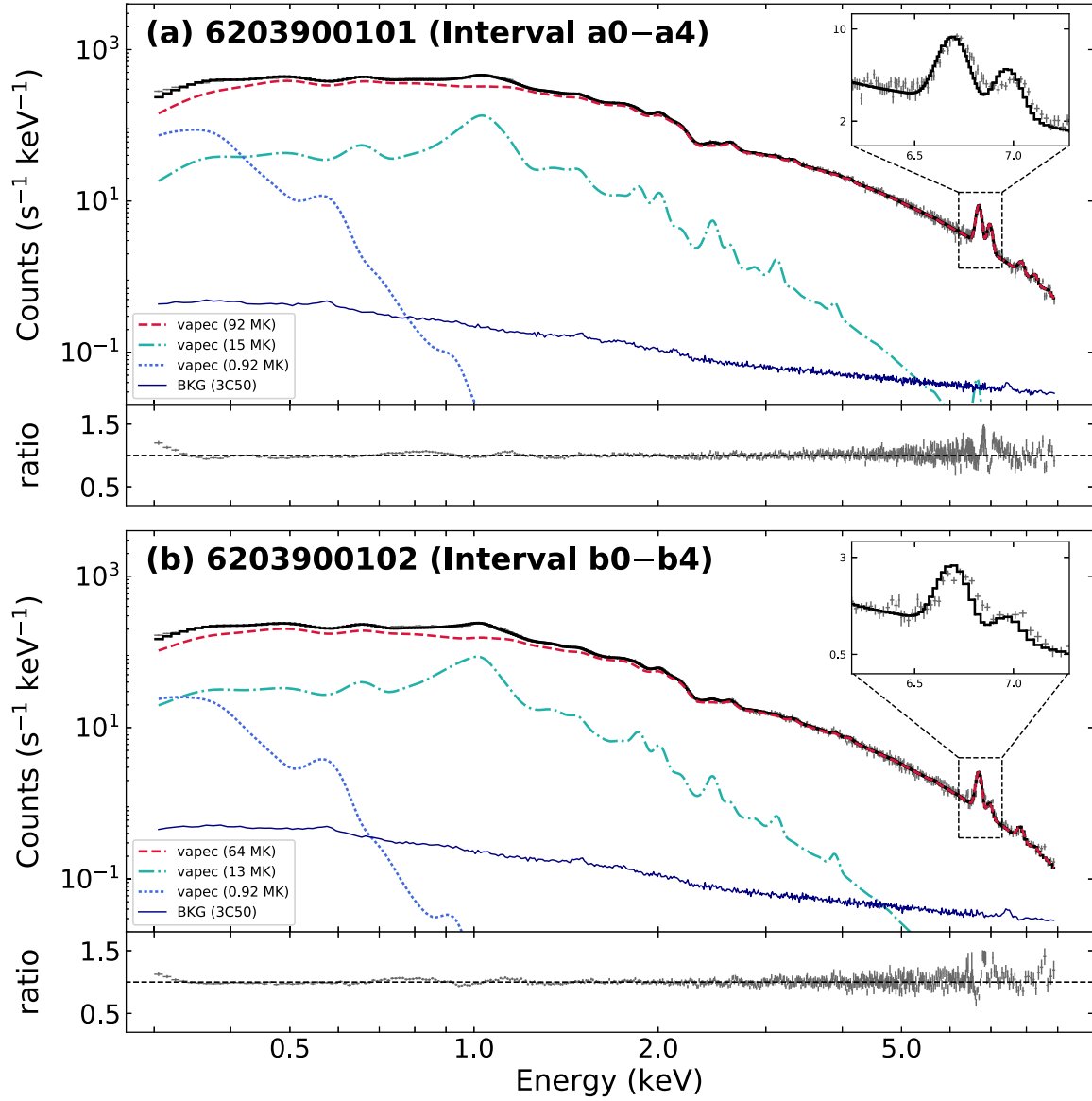


Figure 2. Background-subtracted 0.3–9 keV NICER spectra of IM Peg during the intervals a0–a4 (panel (a), ObsID 6203900101) and b0–b4 (panel (b), ObsID 6203900102). The best-fit models using the three-temperature CIE components (*vaepec*) are shown by the solid black line, composed of 92 MK (red dashed), 15 MK (green dashed-dotted), and 0.92 MK (blue dotted) for panel (a) and 64 MK (red dashed), 13 MK (green dashed-dotted), and 0.92 MK (blue dotted) for panel (b). The navy solid lines show the background spectra calculated with the 3C50 model. The right upper inset panels show the enlarged spectra around the iron emission lines. The lower panels in (a) and (b) are the ratio of the observed data relative to the best-fit model.

resolve the fine structures of the Fe XXV $\text{He}\alpha$ and Fe XXVI $\text{Ly}\alpha$ lines; the former consists of the resonance, intercombination, and forbidden lines at 6.60–6.72 keV, whereas the latter consists of $\text{Ly}\alpha_1$ and $\text{Ly}\alpha_2$ lines at 6.95–6.97 keV (Appendix A). Therefore, both lines are approximated by a single Gaussian function with their lab-frame line centers at ~ 6.69 keV ($\text{He}\alpha$) and ~ 6.97 keV ($\text{Ly}\alpha$).

The simple CIE model fits show residuals around the iron line emissions (6–7 keV) in the ObsID-averaged spectra (intervals a0–a4 and b0–b4 in Figure 2). The highest-temperature component of the CIE model successfully explains the high-energy continuum above 5 keV but fails to reproduce the line profiles (the ratio panels in Figure 2). The enlarged spectra around the iron emission lines in Figure 2 suggest that they are blueshifted. To investigate the time evolution of these two iron emission lines, we further extracted eight spectra of the intervals a0–b4 (see Appendix B). Then, we found the most pronounced

residuals around the iron emission lines appeared in the interval b1 spectrum. Neither the CIE nor off-CIE models can explain the 5–9 keV spectrum during the interval b1 without assuming that the iron emission lines were blueshifted, which suggests that the plasma is moving toward us (Appendix C).

In the following analysis, we focus on the spectral fits around the iron features in 6–7 keV. In Figure 3(a), we analyzed the interval b1 spectrum with a phenomenological model ($\text{power-law} + \text{gauss1} + \text{gauss2}$) in narrowband (5–9 keV). The best-fit parameters of the line centers of the *gauss1* and *gauss2* components were $E_l^{\text{gauss1}} = 6.74 \pm 0.01$ keV and $E_l^{\text{gauss2}} = 6.96 \pm 0.08$ keV, respectively (Table 1). To investigate how far these results deviate from the lab-frame ones, we modeled the CIE spectrum (Figure 3(b)) and convolved it with the NICER response functions (Figure 3(c)) at the electron temperature of the interval b1 with PyAtomDB (Foster & Heuer 2020). In this process, we used Response Matrix File and Ancillary Response

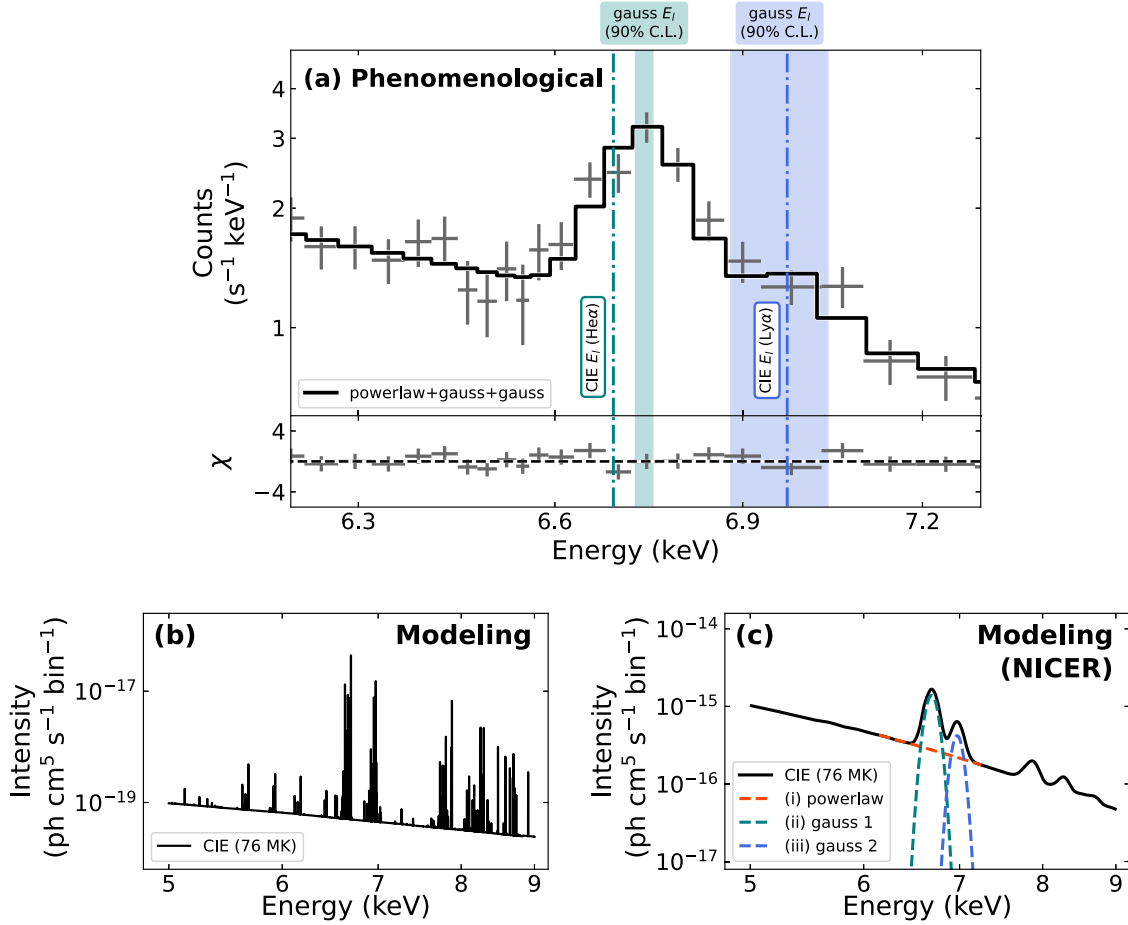


Figure 3. (a) The interval b1 spectrum fitted with a phenomenological model (powerlaw+Gauss+Gauss). The vertical green and blue dashed–dotted lines indicate the line center of He α and Ly α emission lines at the rest frame in the CIE model, respectively. The green and blue shaded areas show the 90% error range of the line center of the two Gaussians. (b) Theoretically expected CIE spectrum during the interval b1 at the electron temperature of $T_e^{\text{b1}} \sim 76$ MK calculated with PyAtomDB. (c) Same spectrum as panel (b) folded by the NICER response function.

Table 1

Best-fit Spectral Parameters of the Phenomenological Model during the Interval b1

Phenomenological Model (powerlaw+gauss1+gauss2)			
powerlaw	Γ		2.21 ± 0.18
	K^{powerlaw} (keV $^{-1}$ cm $^{-2}$ s $^{-1}$)		0.28 ± 0.07
gauss1	E_l^{gauss1} (keV)		6.74 ± 0.01
	σ (keV)		0.00 (fix)
	K^{gauss1} (10 $^{-3}$ cm $^{-2}$ s $^{-1}$)		1.25 ± 0.19
gauss2	E_l^{gauss2} (keV)		6.96 ± 0.08
	σ (keV)		0.00 (fix)
	K^{gauss2} (10 $^{-3}$ cm $^{-2}$ s $^{-1}$)		0.29 ± 0.14
χ^2 (degrees of freedom)			49 (72)
Null hyp. prob.			0.98

Note. The unit of K^{powerlaw} is photons keV $^{-1}$ cm $^{-2}$ s $^{-1}$ at 1 keV, whereas K^{gauss} is the total photons cm $^{-2}$ s $^{-1}$ in the line. The negative velocity indicates that the spectrum is blueshifted.

File made for the interval b1 event file with `nicerl3-spect` (Section 2). During the interval b1, the continuum fitting with `apecc`, ignoring the iron line bands (i.e., 5–9 keV except for 6.3–7.4 keV), gives its electron temperature at $T_e^{\text{b1}} = 76$ MK. We also fit the model spectrum (Figure 3(c)) with the phenomenological model (powerlaw+gauss1+gauss2) and get the

best-fit parameters of $E_l^{\text{He}\alpha}(T_e^{\text{b1}}) = 6.69$ keV and $E_l^{\text{Ly}\alpha}(T_e^{\text{b1}}) = 6.97$ keV. Given these results, the energy shifts of the Fe XXV He α and Fe XXVI Ly α lines are calculated as $\Delta E^{\text{He}\alpha} = E_l^{\text{gauss1}} - E_l^{\text{He}\alpha}(T_e^{\text{b1}}) = 0.05 \pm 0.01$ keV and $\Delta E^{\text{Ly}\alpha} = E_l^{\text{gauss1}} - E_l^{\text{He}\alpha}(T_e^{\text{b1}}) = -0.01 \pm 0.08$ keV, respectively. The Doppler velocity of $v^{\text{He}\alpha} = -c\Delta E^{\text{He}\alpha}/E_l^{\text{He}\alpha}(T_e^{\text{b1}}) = -2200 \pm 600$ km s $^{-1}$ (90% confidence level) overwhelmingly exceeded the escape velocity of IM Peg (-230 km s $^{-1}$). On the other hand, the error range of $v^{\text{Ly}\alpha} = -c\Delta E^{\text{Ly}\alpha}/E_l^{\text{Ly}\alpha}(T_e^{\text{b1}}) = 500 \pm 3500$ km s $^{-1}$ was so large that we could not quantitatively confirm a blueshift of the Fe XXVI Ly α line.

Using the same procedure, we also estimated the electron temperature and the Doppler velocity of the Fe XXV He α and Fe XXVI Ly α lines for all intervals. Figures 4(a)–(e) show the time evolution of physical parameters obtained by our narrowband (5–9 keV) spectral analysis. The electron temperature and intensities (normalizations) of the two lines decrease with time, while the line intensity ratio (Fe XXVI Ly α /Fe XXV He α) stays constant within errors. These results are consistent with the superflare of the RS CVn-type star UX Ari reported in Kurihara et al. (2024). One interesting point is that there was a sign of reheating only during the interval b0 (Figure 4(b)). Figure 4(e) shows that there is a tendency for the line center of the Fe XXV He α line to be blueshifted except for the interval b4. The velocity has a peak value of -2200 ± 600 km s $^{-1}$ at the

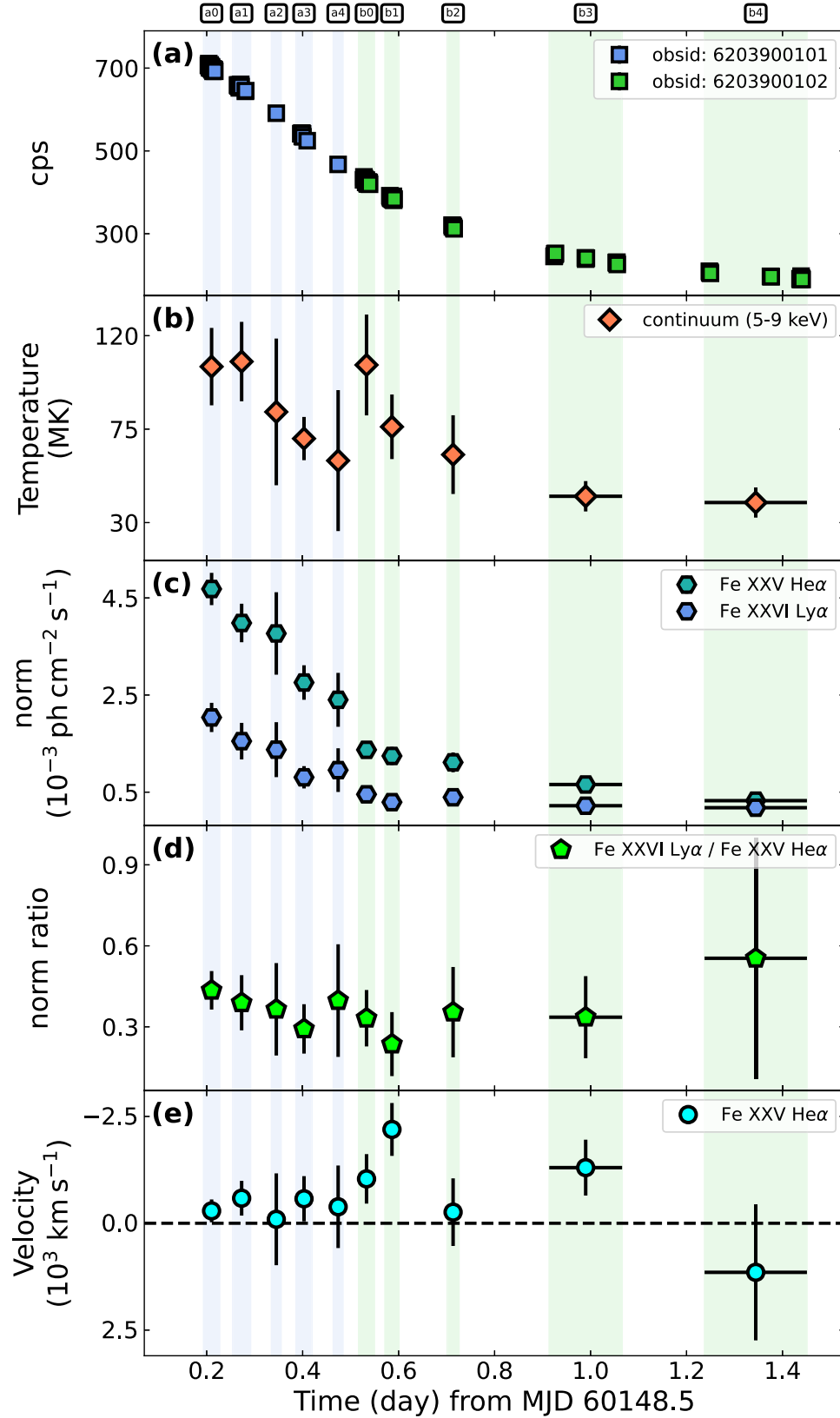


Figure 4. (a) 0.3–4 keV light curve (same as the one in Figure 1(b)). (b) Time evolution of the electron temperature calculated from the 5–9 keV continuum. (c) Best-fit normalization ($K^{\text{gauss}1}$, $K^{\text{gauss}2}$) of the two Gaussians. (d) Ly α /He α ratio calculated using the two Gaussian best-fit normalizations ($K^{\text{gauss}2}/K^{\text{gauss}1}$). (e) Doppler velocity of the line center of the Fe XXV He α line. The negative sign corresponds with blueshift.

interval b1. The intervals other than b1 where the blueshift was clearly identified were the intervals b0 and b3, with velocities of $-1000 \pm 500 \text{ km s}^{-1}$ and $-1300 \pm 650 \text{ km s}^{-1}$, respectively.

In order to detect the blueshift at the 50 eV level, it is also essential to check the energy calibration of the detector. As a reference of a relative energy shift among the NICER

observational data, we selected supernova remnant Cas A, which has been frequently observed by NICER. This source has a similar X-ray intensity as IM Peg during the flare, has the prominent iron Fe XXV He α emission line, and is not time varying. We extracted 605 spectra with the same exposure as each GTI of IM Peg, whose spectra are individually fitted. The 605 Fe XXV He α emission line center follows the Gaussian distribution with a central value of $6.602^{+0.00047}_{-0.00015}$ keV, which is a reasonable value for the Fe XXV He α line and within the range reported by previous satellite observations (6.56–6.62 keV; Appendix D). The width of the Gaussian distribution of these 605 samples is 8.7 eV (26 eV at 3σ , equivalent to 1200 km s^{-1}), which is sufficiently smaller than the velocity discussed in this Letter. We also confirmed that the light leak had little impact on the NICER data since most of our observations (intervals a0–a4, b0–b4) were performed during orbit-night with low background. Undershoot values were below $\sim 10 \text{ counts s}^{-1}$. Furthermore, the NICER team has been checking time-dependent instrumental gain shifts of NICER detectors from 2018 to 2021. They suggest the shift in 2023 is at most 10–15 eV near the Fe–K line energy band (private communication with Dr. Craig Markwardt as the lead of NICER calibration activities). This instrumental gain shift is smaller than the detected $\sim 50 \text{ eV}$ blueshift.

4. Discussion and Conclusion

We present observations of a superflare of the RS CVn-type star IM Peg with NICER from 16:52 UT on 2023 July 23. During the early intervals of the observations, NICER spectra clearly showed Fe XXV He α and Fe XXVI Ly α emission lines. The Fe XXV He α line was blueshifted during the flare, which suggests that the plasma is moving toward us. By phenomenological fitting and CIE modeling, the maximum Doppler velocity of the Fe XXV He α line was estimated to be $-2200 \pm 600 \text{ km s}^{-1}$.

This measurement allows us to estimate the total kinetic energy of the blueshifted plasma, which could lead to understanding global energetics of superflares (see Emslie et al. 2012). The flare loop size is estimated to be $L_{\text{SY}} \sim 10^{-1} R$ using the magnetic reconnection model equations in Shibata & Yokoyama (2002), assuming that the temperature and emission measure of the interval a0 (Figure B1(a)) are the peak values. We assumed that the coronal density is $n_e = 10^{10-13} \text{ cm}^{-3}$ (Aschwanden & Benz 1997; Güdel 2004; Reale 2007; Sasaki et al. 2021) in this calculation. Then, we calculated the kinetic energy of the blueshift as $E_{\text{kin}}^{\text{He}\alpha} \sim L_{\text{SY}}^3 n_0 m_p (v^{\text{He}\alpha})^2 \sim 10^{36} \text{ erg}$, where m_p is the mass of the proton. The estimated kinetic energy is less than a few percent of the X-ray flare energy of $5 \times 10^{37} \text{ erg}$ (Iwakiri et al. 2023).

There are two possible cases for interpreting the blueshifted Fe XXV He α line: a CME or chromospheric evaporation. In the CME interpretation, the $\sim -2200 \text{ km s}^{-1}$ blueshifts of the Fe XXV He α line originate from a CME. The typical velocity of chromospheric evaporation is $\sim -100 \text{ km s}^{-1}$ (e.g., Doschek et al. 1980). The velocity of solar CMEs ($-20 \sim -3000 \text{ km s}^{-1}$; Webb & Howard 2012) can explain the observed velocity. The CME, whose velocity overwhelmingly exceeded the escape velocity ($\sim -230 \text{ km s}^{-1}$), would certainly have flown outward from the star. Furthermore, we see that there is a trend of acceleration from the intervals a4–b1 (Figure 4(g)). This is consistent with Argiroffi et al. (2019), in which they discussed a blueshift during the postflare phase as the CME.

It is also possible that the blueshifted emission from the CME was present during the intervals a0–a4 as well as b1 but was not clearly observed due to the predominance of strong emission from the flare component. In this interpretation, we can also fit the Fe XXV He α line with two Gaussian components, the flare component and the CME component. In the case, the velocity of the CME was estimated to be $-6100 \pm 900 \text{ km s}^{-1}$ for the intervals a0–a4 and $-4400 \pm 1000 \text{ km s}^{-1}$ for the intervals b0–b4, respectively (Appendix E).

The formation temperature (T_{peak}) of the Fe XXV He α line ($T_{\text{peak}} \sim 60 \text{ MK}$) is higher than that of other stellar CME candidates. Argiroffi et al. (2019) discussed a later blueshift of O VIII line ($T_{\text{peak}} \sim 3 \text{ MK}$) on the G-type star HR9024 as a CME candidate. Chen et al. (2022) reported upflows of 3–16 MK plasma accompanied by decrease of the coronal density on the M-type star EV Lac. The temperature of solar CMEs is also on the order of a few megakelvin (Sheoran et al. 2023). The discovery of the Fe XXV He α line blueshift, which could not be investigated by the Chandra HETG observations (Argiroffi et al. 2019; Chen et al. 2022), means that CMEs on magnetically active stars like RS CVn-type stars consist of hot plasma ($\sim 60 \text{ MK}$).

In the chromospheric evaporation interpretation, the reheating during the interval b0 (Figure 4(d)) 1 hr before the most pronounced blueshift can be well understood. From the intervals a4–b0, the electron temperature rose from 60 to 100 MK over the course of an hour. For some reason, the plasma in the chromosphere may have been rapidly reheated at roughly half a day after the flare peak, causing the high-velocity chromosphere evaporation.

To conclude, this work reported the blueshifts of the Fe XXV He α line during a stellar flare for the first time. Given the impact of CMEs on exoplanets (e.g., Airapetian et al. 2016), it is important to determine whether such blueshifts are attributed to a CME or chromospheric evaporation. To know the answer, we need to distinguish whether the line itself is blueshifted or nonshifted and blueshifted components are added together. The high-resolution spectroscopy of X-Ray Imaging and Spectroscopy Mission (XRISM; Tashiro et al. 2020) with its microcalorimeter Resolve (Ishisaki et al. 2018) will enable us to observe the line profile of iron emission lines and distinguish them.

Acknowledgments

NICER analysis software and data calibration were provided by the NASA NICER mission and the Astrophysics Explorers Program. We thank K. Shibata (Doshisha University), H. Maehara (NAOJ), and K. Namekata (Kyoto University) for their useful comments and discussions. We thank C. Markward (NASA/GSFC) for the calibration comments. This research is supported by JSPS KAKENHI grant No. 24KJ1483 (S.I.). T.E. was supported by the RIKEN Hakubi project. Y.N. acknowledges support from NASA ADAP award program No. 80NSSC21K0632. K.H. was supported by NASA under award number 80GSFC21M0002.

Facility: NICER (Gendreau et al. 2016)

Software: astropy (Astropy Collaboration et al. 2013, 2018), HEASoft, Xspec (Arnaud 1996), PyXspec (Gordon & Arnaud 2021), PyAtomDB (Foster & Heuer 2020).

Appendix A

Fine Structure of the Fe XXV He α and XXVI Ly α Lines

We display the line center energy of all lines of the Fe XXV He α and Ly α lines in Table A1 (see Table 1 of Bianchi et al.

Table A1
Line Center Energy of the Fe XXV He α and Ly α Lines

Ion	E_l^{NICER} (keV)	Line ID	Line Energy (keV)
Fe XXV	~ 6.69	w	6.700
		x	6.682
		y	6.668
		z	6.637
Fe XXVI	~ 6.97	Ly α_1	6.973
		Ly α_2	6.952

Note. E_l^{NICER} means the line center energy in the NICER spectra after convolving with the detector response. The values of line energy are taken from Bianchi et al. (2005) and Wargelin et al. (2005).

2005). As mentioned in Section 3, these fine structures are not resolved in the NICER spectra.

Appendix B Wide-band Spectra

We provide wide-band (0.3–9.0 keV) spectra of the intervals a0, b1, and b4 fitted with the three-temperature CIE models

(vapec) as examples in Figure B1. The interval a0 spectrum with the best photon statistics showed the slight systematic residuals around iron emission lines, which were not as much as the interval b1. The interval b1 spectrum showed the most pronounced residuals around iron emission lines as discussed in Section 3. The interval b4 spectrum with the relatively poor photon statistics showed no systematic residuals around iron emission lines. This is consistent with the fact that the Doppler velocity of the interval b4 spectrum obtained by our narrowband spectral analysis (Figure 4(e)) was not blueshifted.

Appendix C Fitting the Interval b1 Spectrum with Plasma Models

We also tried CIE (apec) and off-CIE plasma models and the ionizing (nei) and recombining (rnei) models for the interval b1 spectrum. When we used the recombining model, we fixed the initial temperature to the electron temperature of the interval a0 of ~ 105 MK. All models cannot eliminate the residuals at $v = 0$ (Figures C1(a)–(c)). On the other hand, when we leave the velocity v free and again fit the spectrum with apec, nei, and rnei (Figures C1(d)–(f)), bulk motion, and thus the blueshifted line center corresponding with the negative sign of the velocity, improved the fittings with better p -values, eliminating the residuals (Table C1). The best-fit parameters of

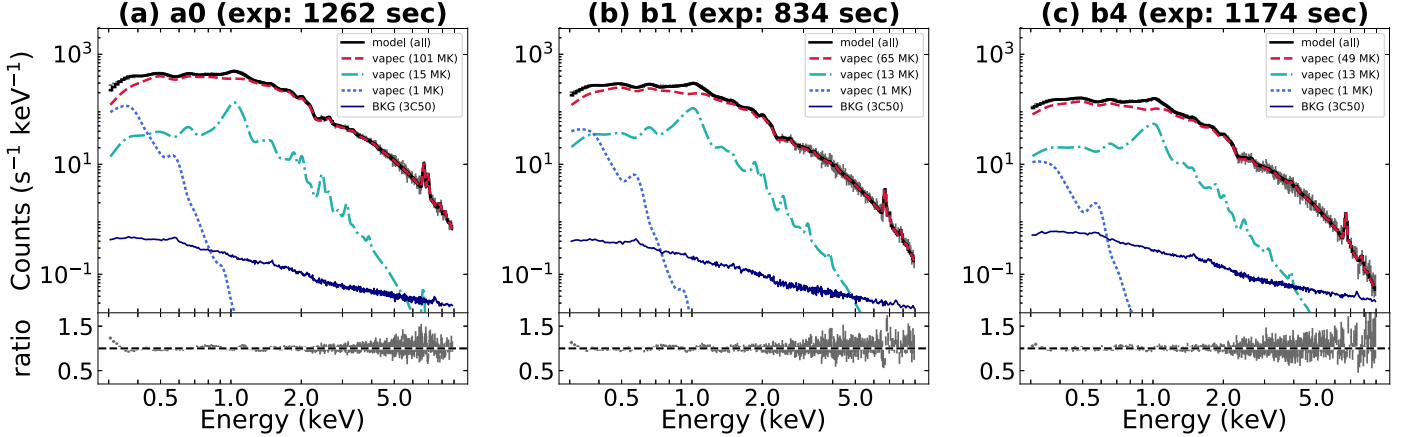


Figure B1. Same as Figure 2 but during the intervals a0, b1, and b4 for panels (a), (b), and (c), respectively. The temperatures of the three components are 101, 15, and 1 MK for panel (a); 65, 13, and 1 MK for panel (b); and 49, 13, and 1 MK for panel (c).

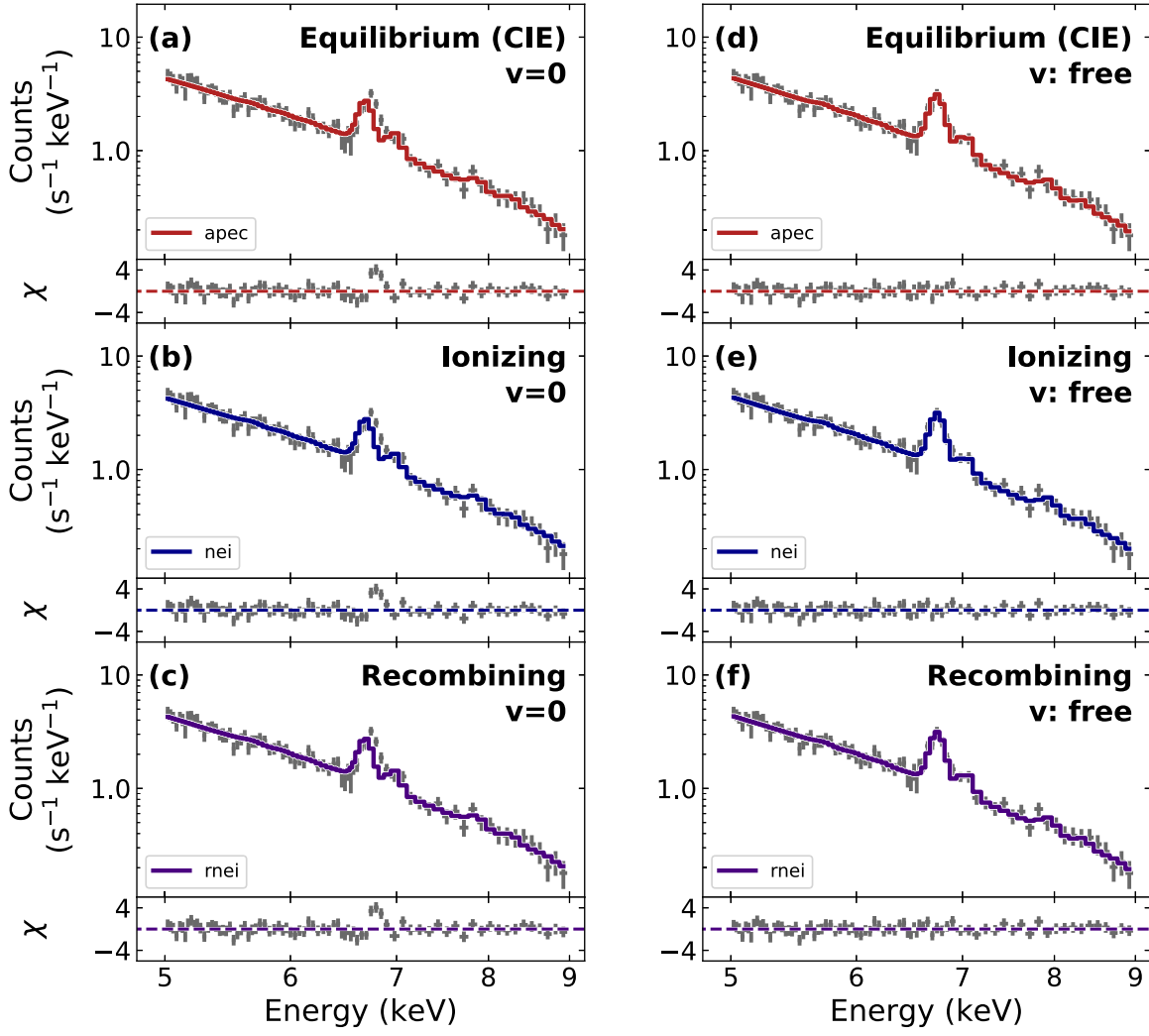


Figure C1. Comparison of spectral fittings using different plasma models around the iron emission lines during the interval b1: the CIE (*apec*, panel (a)); ionizing (*nei*, panel (b)); and recombining (*rnei*, panel (c)) plasma models with the velocity fixed at $v = 0$. The lower panels show the fitting residuals. Panels (d), (e), and (f) are the same as panels (a), (b), and (c), respectively, but letting the velocity of the plasma free.

the velocity were $-2540 \pm 680 \text{ km s}^{-1}$, $-2450 \pm 460 \text{ km s}^{-1}$, and $-2630 \pm 530 \text{ km s}^{-1}$ for *apec*, *nei*, and *rnei*, respectively. These values are consistent with the velocity of $-2200 \pm 600 \text{ km s}^{-1}$ obtained with the phenomenological fitting (Section 3) within error bars. Furthermore, the best-fit parameters of temperature, abundance, velocity, and normalization became

consistent within error bars among the three plasma models. This suggests that the observed 5–9 keV spectra can be explained either by CIE or off-CIE plasma models, assuming the plasma moves at a velocity of about -2500 km s^{-1} . In other words, no model can reproduce the observed iron emission lines without the blueshifts.

Table C1
Best-fit Spectral Parameters of Plasma Models during the Interval b1

Collisional Ionization Equilibrium Plasma Model (apec)					
Velocity: fixed at zero			Velocity: free		
apec	kT (keV)/ T (MK)	$6.90 \pm 0.69 / 80.0 \pm 8.0$	apec	kT (keV)/ T (MK)	$6.16 \pm 0.65/71.5 \pm 7.54$
	Z (Z_{\odot})	0.25 ± 0.05		Z (Z_{\odot})	0.28 ± 0.05
	v (10^3 km s^{-1})	0.00 (fixed)		v (10^3 km s^{-1})	-2.54 ± 0.68
	K^{apec}	0.49 ± 0.04		K^{apec}	0.51 ± 0.05
	χ^2 (d.o.f.)	86 (75)		χ^2 (d.o.f.)	45 (74)
	Null hyp. prob.	0.17		Null hyp. prob.	0.99
Ionizing Plasma Model (nei)					
Velocity: fixed at zero			Velocity: free		
nei	kT (keV)/ T (MK)	$8.01 \pm 1.67/92.9 \pm 19.4$	nei	kT (keV)/ T (MK)	$6.74 \pm 1.12/78.2 \pm 13.0$
	Z (Z_{\odot})	0.24 ± 0.06		Z (Z_{\odot})	0.28 ± 0.05
	$n_e t$ (s cm^{-3})	$\gtrsim 2 \times 10^{12}$		$n_e t$ (s cm^{-3})	$\gtrsim 2 \times 10^{11}$
	v (10^3 km s^{-1})	0.00 (fixed)		v (10^3 km s^{-1})	-2.45 ± 0.46
	K^{nei}	0.46 ± 0.06		K^{nei}	0.49 ± 0.06
	χ^2 (d.o.f.)	86 (74)		χ^2 (d.o.f.)	44 (73)
	Null hyp. prob.	0.16		Null hyp. prob.	0.99
Recombining Plasma Model (rnei)					
Velocity: fixed at zero			Velocity: free		
rnei	kT (keV)/ T (MK)	$7.00 \pm 0.76/81.2 \pm 8.81$	rnei	kT (keV)/ T (MK)	$6.18 \pm 0.68/71.7 \pm 7.89$
	kT_{init} (keV)/ T_{init} (MK)	9.06/105		kT_{init} (keV)/ T_{init} (MK)	9.06/105
	Z (Z_{\odot})	0.25 ± 0.05		Z (Z_{\odot})	0.29 ± 0.05
	$n_e t$ (s cm^{-3})	$\gtrsim 5 \times 10^{11}$		$n_e t$ (s cm^{-3})	$\gtrsim 6 \times 10^{12}$
	v (10^3 km s^{-1})	0.00 (fixed)		v (10^3 km s^{-1})	-2.63 ± 0.53
	K^{rnei}	0.49 ± 0.04		K^{rnei}	0.51 ± 0.03
	χ^2 (d.o.f.)	87 (74)		χ^2 (d.o.f.)	44 (73)
	Null hyp. prob.	0.15		Null hyp. prob.	0.99

Note. The lower limits of $n_e t$ in nei and rnei models are evaluated from the two-dimensional contour plots of $(kT, n_e t)$ as the 90% confidence interval. K^{apec} , K^{nei} , and K^{rnei} mean $10^{-14}(4\pi)^{-1}[D_A(1+z)]^{-2} \int n_e n_H dV$, where D_A is the angular diameter distance to the source, z is the redshift, n_e and n_H are the electron and hydrogen densities, and dV is the volume element.

Appendix D

Energy Determination Accuracy of NICER around Iron Emission Lines

As discussed in Section 3, the Fe XXV He α line seemed to be blueshifted during the flare. However, the accuracy of the NICER response function in determining the energy of photons should be checked. Therefore, we need to investigate how much uncertainty the NICER response function has and whether the observed blueshifts are attributed to the astronomical phenomenon.

We analyzed a large number of NICER data (192 ObsIDs) of the supernova remnant Cas A (e.g., Holt et al. 1994; Maeda et al. 2009), which has a count rate comparable to that of IM Peg during the flare, a strong iron emission line, and no time variability. We downloaded all Cas A data observed by NICER from the HEASARC archive and processed them in the same manner as described in Section 2. Then, we extracted GTI-divided and all-GTI spectra from all ObsID data. As shown in Figures D1(a)–(c), we fitted the spectra, whose exposure times are $500 < t_{\text{exp}} < 1500$ s, in 5–7.4 keV with the phenomenological model (powerlaw+Gauss). The exposure time of most intervals during the flare on IM Peg

is in this range. The total number of Cas A spectra we fitted was 605.

Figure D1(d) shows the distribution of the line center of the Gaussian. The median value of the line center was $E_{\text{med}} = 6.602$ keV. The central value and standard deviation of ΔE ($=E - E_{\text{med}}$) were $\mu = (1.6 \pm 3.1) \times 10^{-4}$ keV and $\sigma = (8.7 \pm 0.3) \times 10^{-3}$ keV, respectively. The error ranges of μ and σ are at 90% confidence level. Holt et al. (1994) reported the difference in the Doppler shift between the locations in Cas A. According to their observations with the ASCA Observatory, the range of the line center energy of the iron emission line is 6.5568–6.6080 keV (see Table 1 in Holt et al. 1994). On the other hand, Maeda et al. (2009) showed the line center energy is 6.621 keV from the spectrum extracted from the entire Cas A observed with Suzaku. The NICER 90% confidence level of the line center in our analysis ($6.60185 \text{ keV} < E_{\text{med}} + \mu < 6.60247 \text{ keV}$) is in the range of these previous works. Furthermore, our results indicate that the upper limit of the uncertainty of the NICER response function is limited to $|\Delta E| \lesssim 3\sigma = 2.6 \times 10^{-2}$ keV, which corresponds to the Doppler velocity $v \sim \pm 1200 \text{ km s}^{-1}$. This means that the $-2200 \pm 600 \text{ km s}^{-1}$ ($(5 \pm 1) \times 10^{-2}$ keV) blueshift detected

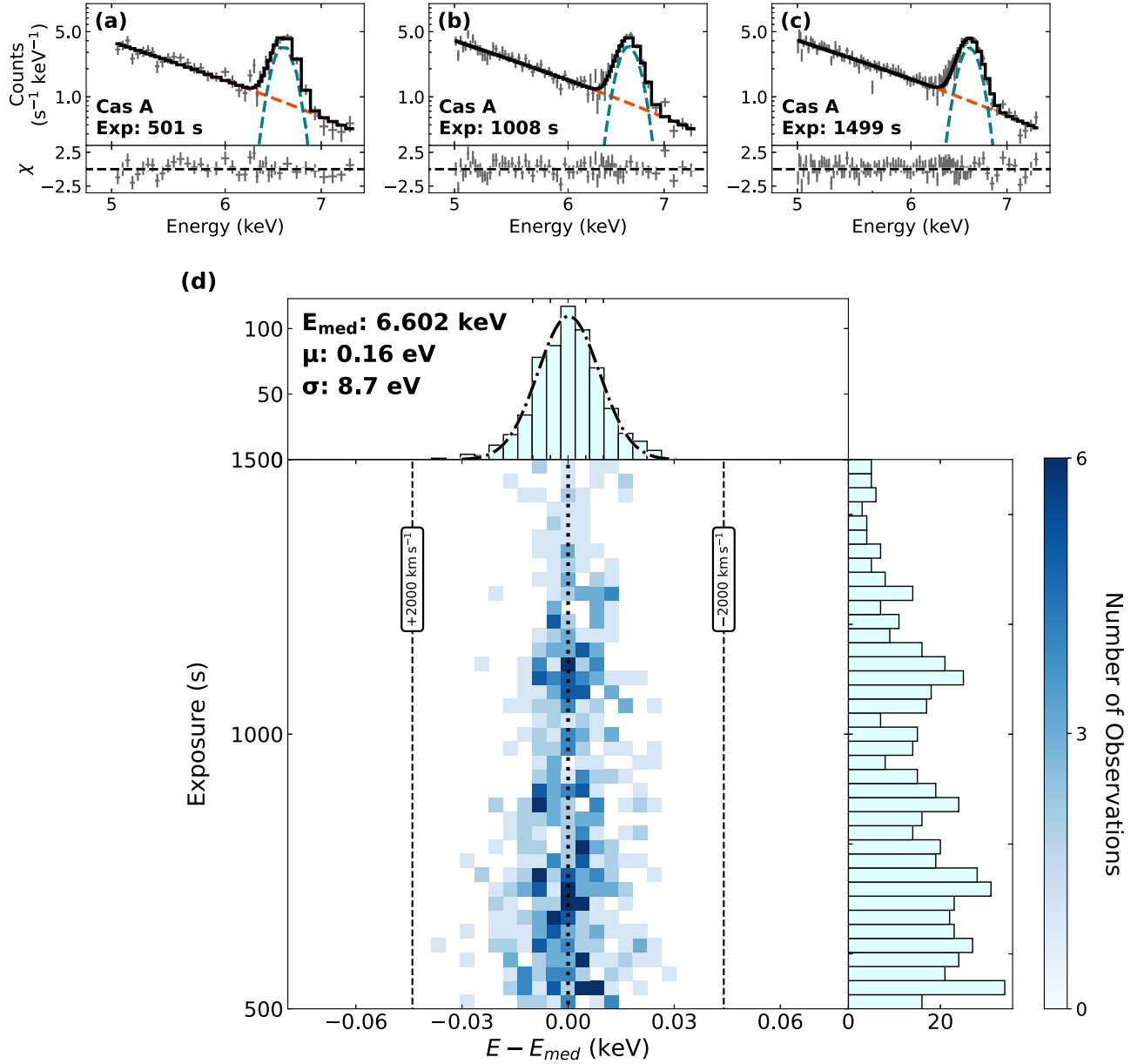


Figure D1. (a)–(c) Examples of NICER Cas A spectra fitted with the phenomenological model of `powerlaw+Gauss`, whose exposure times are (a) ~ 500 s, (b) ~ 1000 s, and (c) ~ 1500 s, respectively. Orange and green dashed lines indicate `powerlaw` and `Gauss` components, respectively. (d) The distribution of the line center of the Gaussian function ($\Delta E = E - E_{\text{med}}$). The upper panel shows the histogram of the distribution for all data ($N = 605$) and the Gaussian fitting (black dashed-dotted line). The color map shows the distribution at each range of the exposure time. The right panel shows the histogram of the distribution at each exposure time.

during the interval b1($t_{\text{exp}} = 834$ sec) cannot be explained by the uncertainty of the NICER energy determination.

Furthermore, since we were multiplying both modeling and observed spectra by the response files at each time and taking the difference of the line center between them (Section 3), the response-derived Doppler shift should cancel out to some extent. Given these considerations, it is highly possible that the astronomical phenomenon made the observed blueshifts.

Appendix E

Fitting the Fe XXV He α Line with Two Gaussian Components

When we consider the blueshifts of the Fe XXV He α line being attributed to a CME, it is physically reasonable that

there are both nonshifted (flare) and blueshifted (CME) components of the Fe XXV He α line as discussed in the case of the blueshifted H α line (e.g., Inoue et al. 2023). Thus, we also fitted the intervals a0–a4 and b0–b4 spectra with the phenomenological model (`powerlaw+Gauss*3`) considering the CME components (Figure E1). We did not fit the individual interval spectra with this model because photon statistics are insufficient to determine the CME components. We fixed the line centers of the flare components of the Fe XXV He α and Fe XXVI Ly α lines to the lab-frame ones. As a result, the best-fit values of the line centers of the CME components of the Fe XXV He α line were 6.83 ± 0.02 keV and 6.79 ± 0.02 keV during intervals a0–a4 and b0–b4, respectively. These values correspond

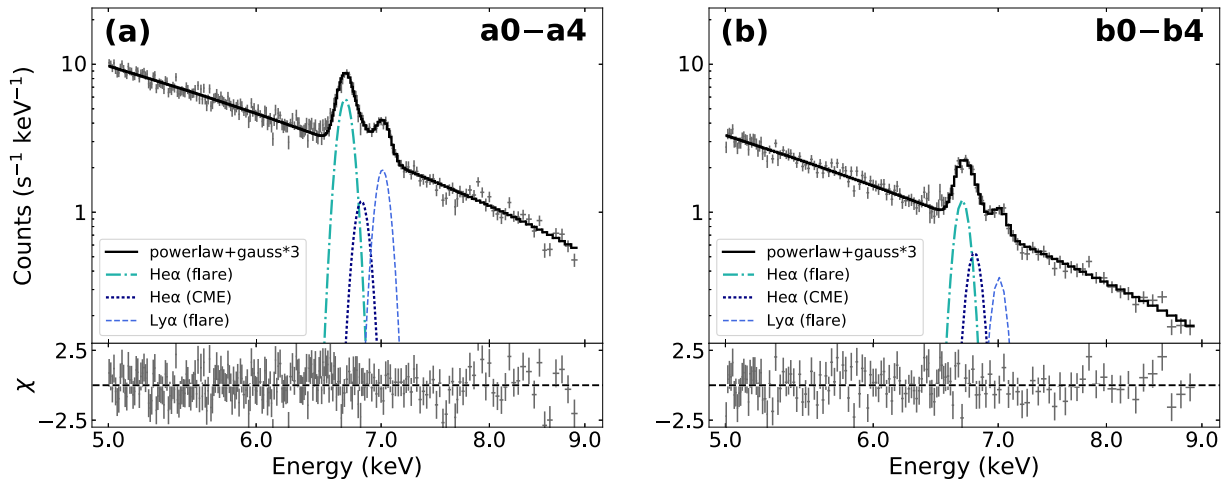


Figure E1. Background-subtracted 5–9 keV spectra of IM Peg fitted with a phenomenological model (powerlaw+Gauss*3) during the intervals a0–a4 and b0–b4 for panels (a) and (b), respectively. Green dashed–dotted and blue dashed lines correspond to the Fe XXV He α and the Fe XXVI Ly α lines, respectively, whose line centers are fixed to the values in the laboratory frame. Navy dotted lines indicate the blueshifted components of the Fe XXV He α line.

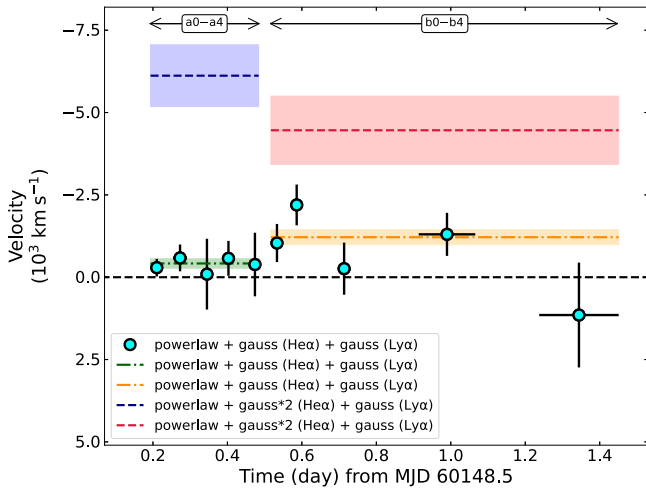


Figure E2. Doppler velocity of the blueshifted components of the Fe XXV He α line (see, e.g., Figure E1) overlaid on that of the line center of the Fe XXV He α line shown in Figure 4(g). Navy and red dashed lines indicate the Doppler velocity of the blueshifted components of the Fe XXV He α line with the 90% error range during the combined intervals a0–a4 and b0–b4, respectively, when we fit the spectra with powerlaw+Gauss*3 model. Green and orange dashed–dotted lines indicate the Doppler velocity of the line center of the Fe XXV He α line with the 90% error range during the combined intervals a0–a4 and b0–b4, respectively, when we fit the spectra with the powerlaw+Gauss*2 model.

to the Doppler velocities of $-6100 \pm 900 \text{ km s}^{-1}$ and $-4400 \pm 1000 \text{ km s}^{-1}$, respectively (Figure E2).

ORCID iDs

Shun Inoue <https://orcid.org/0000-0003-3085-304X>
 Wataru Buz Iwakiri <https://orcid.org/0000-0002-0207-9010>
 Teruaki Enoto <https://orcid.org/0000-0003-1244-3100>
 Hiroyuki Uchida <https://orcid.org/0000-0003-1518-2188>
 Miki Kurihara <https://orcid.org/0000-0002-3133-9053>
 Masahiro Tsujimoto <https://orcid.org/0000-0002-9184-5556>
 Yuta Notsu <https://orcid.org/0000-0002-0412-0849>
 Kenji Hamaguchi <https://orcid.org/0000-0001-7515-2779>
 Keith Gendreau <https://orcid.org/0000-0001-7115-2819>
 Zaven Arzoumanian <https://orcid.org/0009-0008-6187-8753>
 Takeshi Go Tsuru <https://orcid.org/0000-0002-5504-4903>

References

- Airapetian, V. S., Glocer, A., Gronoff, G., Hébrard, E., & Danchi, W. 2016, *NatGe*, **9**, 452
- Airapetian, V. S., Barnes, R., Cohen, O., et al. 2020, *IJAsB*, **19**, 136
- Argiroffi, C., Reale, F., Drake, J. J., et al. 2019, *NatAs*, **3**, 742
- Arnaud, K. A. 1996, in ASP Conf. Ser. 101, *Astronomical Data Analysis Software and Systems V*, ed. G. H. Jacoby & J. Barnes (San Francisco, CA: ASP), 17
- Arzoumanian, Z., Gendreau, K. C., Baker, C. L., et al. 2014, *Proc. SPIE*, **9144**, 914420
- Ashwanden, M. J., & Benz, A. O. 1997, *ApJ*, **480**, 825
- Astropy Collaboration, Price-Whelan, A. M., Sipőcz, B. M., et al. 2018, *AJ*, **156**, 123
- Astropy Collaboration, Robitaille, T. P., Tollerud, E. J., et al. 2013, *A&A*, **558**, A33
- Bianchi, S., Matt, G., Nicastro, F., Porquet, D., & Dubau, J. 2005, *MNRAS*, **357**, 599
- Buzasi, D. L., Ramsey, L. W., & Huenemoerder, D. P. 1987, *ApJ*, **322**, 353
- Canizares, C. R., Davis, J. E., Dewey, D., et al. 2005, *PASP*, **117**, 1144
- Caspi, A. 2010, PhD thesis, Univ. of California, Berkeley
- Chen, H., Tian, H., Li, H., et al. 2022, *ApJ*, **933**, 92
- Doschek, G. A., Feldman, U., Kreplin, R. W., & Cohen, L. 1980, *ApJ*, **239**, 725
- Emslie, A. G., Dennis, B. R., Shih, A. Y., et al. 2012, *ApJ*, **759**, 71
- Fisher, G. H., Canfield, R. C., & McClymont, A. N. 1985, *ApJ*, **289**, 425
- Flores Soriano, M., & Strassmeier, K. G. 2017, *A&A*, **597**, A101
- Foster, A. R., & Heuer, K. 2020, *Atoms*, **8**, 49
- Fuhrmeister, B., Czesla, S., Schmitt, J. H. M. M., et al. 2018, *A&A*, **615**, A14
- Gendreau, K. C., Arzoumanian, Z., Adkins, P. W., et al. 2016, *Proc. SPIE*, **9905**, 99051H
- Gendreau, K. C., Arzoumanian, Z., & Okajima, T. 2012, *Proc. SPIE*, **8443**, 844313
- Gordon, C., & Arnaud, K. 2021, PyXspec: Python interface to XSPEC spectral-fitting program, Astrophysics Source Code Library, ascl:2101.014
- Güdel, M. 2004, *A&ARv*, **12**, 71
- Holt, S. S., Gotthelf, E. V., Tsunemi, H., & Negoro, H. 1994, *PASJ*, **46**, L151
- Honda, S., Notsu, Y., Namekata, K., et al. 2018, *PASJ*, **70**, 62
- Inoue, S., Enoto, T., Namekata, K., et al. 2024, *PASJ*, **76**, 175
- Inoue, S., Maehara, H., Notsu, Y., et al. 2023, *ApJ*, **948**, 9
- Ishisaki, Y., Ezoe, Y., Yamada, S., et al. 2018, *JLTP*, **193**, 991
- Iwakiri, W., Hamaguchi, K., Gendreau, K., et al. 2023, *ATel*, **16152**, 1
- Koller, F., Leitzinger, M., Temmer, M., et al. 2021, *A&A*, **646**, A34
- Kurihara, M., Iwakiri, W. B., Tsujimoto, M., et al. 2024, *ApJ*, **965**, 135
- Lu, H.-P., Tian, H., Zhang, L.-Y., et al. 2018, *JLTP*, **163**, A140
- Maeda, Y., Uchiyama, Y., Bamba, A., et al. 2009, *PASJ*, **61**, 1217
- Maehara, H., Notsu, Y., Namekata, K., et al. 2021, *PASJ*, **73**, 44
- Matsuoka, M., Kawasaki, K., Ueno, S., et al. 2009, *PASJ*, **61**, 999
- Muhead, P., Guenther, E. W., Mutabazi, T., & Jurua, E. 2020a, *A&A*, **637**, A13
- Muhead, P., Guenther, E. W., Mutabazi, T., & Jurua, E. 2020b, *MNRAS*, **499**, 5047
- Namekata, K., Airapetian, V. S., Petit, P., et al. 2024, *ApJ*, **961**, 23

- Namekata, K., Maehara, H., Honda, S., et al. 2021, [NatAs](#), **6**, 241
- Notsu, Y., Kowalski, A. F., Maehara, H., et al. 2024, [ApJ](#), **961**, 189
- Reale, F. 2007, [A&A](#), **471**, 271
- Remillard, R. A., Loewenstein, M., Steiner, J. F., et al. 2022, [AJ](#), **163**, 130
- Sasaki, R., Tsuboi, Y., Iwakiri, W., et al. 2021, [ApJ](#), **910**, 25
- Sheoran, J., Pant, V., Patel, R., & Banerjee, D. 2023, [FrASS](#), **10**, 27
- Shibata, K., & Yokoyama, T. 2002, [ApJ](#), **577**, 422
- Sinha, S., Srivastava, N., & Nandy, D. 2019, [ApJ](#), **880**, 84
- Smith, R. K., Brickhouse, N. S., Liedahl, D. A., & Raymond, J. C. 2001, [ApJL](#), **556**, L91
- Tashiro, M., Maejima, H., Toda, K., et al. 2020, [Proc. SPIE](#), **11444**, 1144422
- Testa, P., Drake, J. J., & Peres, G. 2004, [ApJ](#), **617**, 508
- Tsuboi, Y., Yamazaki, K., Sugawara, Y., et al. 2016, [PASJ](#), **68**, 90
- Tsuru, T., Makishima, K., Ohashi, T., et al. 1989, [PASJ](#), **41**, 679
- Vida, K., Kriskovics, L., Oláh, K., et al. 2016, [A&A](#), **590**, A11
- Vida, K., Leitzinger, M., Kriskovics, L., et al. 2019, [A&A](#), **623**, A49
- Wargelin, B. J., Beiersdorfer, P., Neill, P. A., Olson, R. E., & Scofield, J. H. 2005, [ApJ](#), **634**, 687
- Webb, D. F., & Howard, T. A. 2012, [LRSP](#), **9**, 3
- Weisskopf, M. C., Tananbaum, H. D., Van Speybroeck, L. P., & O'Dell, S. L. 2000, [Proc. SPIE](#), **4012**, 2
- Zellem, R., Guinan, E. F., Messina, S., et al. 2010, [PASP](#), **122**, 670